JGR Space Physics

RESEARCH ARTICLE
10.1029/2020JA028281

Properties of Solar Wind Structures at Mercury's Orbit

P. Diego[1], M. Piersanti[2], M. Laurenza[1], and U. Villante[3,4]

[1]INAF-Istituto di Astrofisica e Planetologia Spaziali, Rome, Italy, [2]INFN-University of Rome Tor-Vergata, Rome, Italy, [3]Department of Physical and Chemical Sciences, University of L'Aquila, L'Aquila, Italy, [4]Consorzio Area di Ricerca in Astrofisica, L'Aquila, Italy

Key Points:
- Properties of the different solar wind structures between 0.29 and 0.47 AU are compared
- Alfvénic and sonic Mach number typical values between 0.3 and 1 AU for different solar wind structures are identified
- Highest solar wind dynamic pressures at Mercury orbit, ~15 to 30 nPa, occur during noncompressive density enhancements

Correspondence to:
P. Diego,
piero.diego@iaps.inaf.it

Citation:
Diego, P., Piersanti, M., Laurenza, M., & Villante, U. (2020). Properties of solar wind structures at Mercury's orbit. *Journal of Geophysical Research: Space Physics*, *125*, e2020JA028281. https://doi.org/10.1029/2020JA028281

Received 30 MAY 2020
Accepted 29 AUG 2020
Accepted article online 3 SEP 2020

Abstract Mercury's environment is characterized by a high variability and strength of the solar forcing. Its magnetosphere is completely reconfigured even for small changes in the interplanetary magnetic field and the solar wind (SW) dynamic pressure. Different configurations are due to occurrence of different structures in the SW. Among them, high speed streams from coronal holes, magnetic clouds, and noncompressive density enhancement have been analyzed to better characterize the Hermean conditions, which might be expected during the ongoing BepiColombo mission. Helios 1 and 2 mission data collected between 0.29 and 0.47 AU have been used to perform a statistical analysis of these SW structures. The numerical results reported in the paper, as well as the probability densities displayed in the maps, give more precise indications when associated to a rigorous SW structures selection. The occurrence rate along solar cycle together with the average features of each class of SW structures are useful information for Space Weather topics. Results from the same analysis performed at 1 AU have been used to further verification of the radial behavior of the SW parameters.

1. Introduction

Mercury is the planet closest to the Sun, hence exposed to a highly dense and hot solar wind (SW) and to a strong interplanetary magnetic field (IMF). In addition to that, Mercury has a very eccentric orbit, with a perihelion at 0.31 Astronomical Unit (AU) and an aphelion at 0.47 AU (also called "Mercury's orbit" hereafter), which results in a high variation in the SW and IMF conditions depending on the position of the planet along its orbit (Russell et al., 1988).

Moreover, Mercury is supposed to have a high variable magnetospheric dynamics, due to its magnetic field interaction with the SW as observed by Mariner 10 probe (Korth et al., 2018; Russell et al., 1988; Slavin et al., 2018). A renewed interest in Mercury's environment derives from the space mission MESSENGER (National Aeronautics and Space Administration, NASA) and the ongoing BepiColombo (ESA/JAXA) that will characterize Hermean environment and will observe the effects of solar plasma on both Mercury's surface and magnetosphere. This will give a strong contribution in the comprehension of solar perturbation's impacts on planets under different SW regimes. The BepiColombo arrival at Mercury's orbit is planned for the beginning of the Solar Cycle No. 25. Since it is an odd numbered cycle, we can assume having common features with same phase of Cycle No. 21 (i.e., during the HELIOS data acquisition period at small heliocentric distances), in terms of occurrence of SW streams, as far as occurrence and persistence of other interplanetary structures (Cliver et al., 1996).

As for the Earth, the principal SW drivers of the magnetospheric activity are the dynamic pressure and the IMF orientation. Ranges and variability of these parameters are expected to be very different at Mercury's orbit with respect to the Earth's case. In particular, at 0.3–0.5 AU the angle of the IMF with respect to the radial direction is between 18° and 28° for typical SW conditions (Sarantos et al., 2001; Villante et al., 1978).

HELIOS 1 and 2 data were widely used to study SW, IMF, energetic particles, and dust in interplanetary space at different solar distances (e.g., Burlaga, 1996; Mariani et al., 1979; Marsch, 1991). In general, the radial dependence of the IMF has been found in good agreement with Parker's predictions (Villante et al., 1979). Through a statistical analysis over the whole data set of Helios data between 0.31 and 0.47 AU, Russell et al. (1988) found the following average values (< >) and standard deviations (SDs): $<|B|> = 30.5$ nT (SD = 11.2 nT), $<D> = 59.8$ cm^{-3} (SD = 44.4 cm^{-3}), $<V> = 423$ km/s (SD = 112 km/s), $\beta = 0.53$ (SD = 0.71), and $M_a = 5.4$ (SD = 3.2). Anyway, investigating data recorded by several space

missions between 1965 and 1979 at various solar distance (from 0.31 up to 1.52 AU), Slavin and Holzer (1981) improved the radial behavior knowledge for the various SW parameters finding SW density values in the range between 73 cm^{-3} (at 0.31 AU) and 32 cm^{-3} (at 0.47 AU), IMF in the range between 46 and 21 nT and SW proton temperature (T) in the range between 17×10^4 and 13×10^4 K, addressing a characteristic T decrease law of $r^{-2/3}$, not provided by Parker's model. As expected, it can be easily seen that both density and IMF on average decreases as r^{-2}. On the other hand, they found no significant radial decrease for the SW velocity. Burlaga (2001) summarized several aspects of SW variations in the inner heliosphere by analyzing its radial evolution. The results allowed to evaluate changes in the SW structure's features through a direct comparison between measurements performed at about 0.3 and at 1 AU. He found that the magnetic field is ≈3–6 times stronger than the average field strength at 1 AU; the SW speed does not vary significantly with distance between 0.29 and 0.98 AU, with an average value of 460 km/s; the SW density decreases with distance from the Sun as $r^{-(2.1 \pm 0.1)}$.

Sarantos and Slavin (2009), using MESSENGER data, show that sonic and Alfvénic Mach numbers are generally in the range ~2–5, reaching lower values during solar active conditions such as coronal mass ejections (CMES). In extreme cases, the Alfvénic Mach number can reach very low value (~1), leading to the formation of the so called Alfvén wings (Kivelson, 2004, and references therein). Such Mach number values are lower than the Earth's case, where are generally in the range ~7–10 (Marsch et al., 1982).

An important aspect concerns the correct identification of the different SW regimes. In fact, since the early in situ measurements at 1 AU, different average values of SW parameters have been identified for different years (e.g., Gosling et al., 1971). This effect is due to changes in the occurrence of various SW regimes through the solar cycle. Moreover, the impact of each SW regime on Mercury's magnetosphere is expected to be different than the Earth's case because of the weak intrinsic magnetic field of Mercury, the SW plasma parameters, and the orientation of the IMF near the orbit of Mercury (Sarantos & Slavin, 2009). In fact, Raines et al., 2015 found that the concurring contribution of the SW high dynamic pressure and the weak planetary magnetic field moves the dayside magnetospheric boundaries (viz., the bow-shock and magnetopause) approximately 8 times closer to Mercury's surface with respect to the Earth's case.

So, to better understand the dynamics of the Hermean magnetosphere in response to SW plasma and IMF variations, a characterization of the solar inputs is needed (e.g., James et al., 2017; Johnson & Hauck, 2016). For this reason, studies aiming to the evaluation of changes in the shape and in the dynamics of the Hermean magnetosphere should take in proper account that SW variations are not random but depend on the occurrence of specific structures traveling in space.

In general, each SW regime has typical features and can be roughly separated in two categories, related to different solar coronal structures: transient structures, originated from eruptions in the active regions, such as magnetic clouds (MCs) (Burlaga et al., 1981), noncompressive density enhancements (NCDEs) (Gosling et al., 1977), and corotating structures from coronal holes (CH) such as regular high speed streams (HSSs) (e.g., Smith & Wolfe, 1979).

In this paper, we outline the features of solar forcing at Mercury's orbit through a statistical analysis of the SW parameters distributions between 0.29 and 0.47 AU by using both plasma and magnetic field observations from Helios. In addition, we analyze single classes of structures in order to identify the typical values of SW parameters for different regimes and assess their variability with the radial distance.

The paper is organized as follows: Section 2 describes the data set used, its global features, and the criteria used to select SW structures; section 3 discusses the results obtained for the statistical analysis of SW parameters for the different classes of interplanetary structures; section 4 reports the differences with the Earth's orbit; and section 5 presents the conclusions.

2. Data Description and Event Selection

In order to investigate SW regimes at Mercury's orbit, we used hourly data from HELIOS 1 (H1) and HELIOS 2 (H2) missions. Their orbital period (trajectory around the Sun) was about 6 months, of which about 35 days between 0.29 and 0.47 AU (Mariani et al., 1983). HELIOS measurements were recorded during the minimum phase of Solar Cycle No. 20 and the ascending phase of Solar Cycle No. 21; we refer here to plasma experiment (Exp. 1—H. Rosenbauer and R. Schwen) and magnetic field experiment (Exp. 3—F. Mariani

Table 1
Averages of Unperturbed Periods at Different Solar Distance

	Distance (AU)	$\|B\|$ (nT)	V (km/s)	D (cm^{-3})	T (K)
Average	[0.29;0.42]	37.3	384.2	60.4	19.8×10^4
SD		7.7	50.7	23.5	9.8×10^4
N		712	712	712	712
Average	[0.29;0.32)	42.1	368.8	69.2	19.0×10^4
SD		5.9	49.9	22.8	11.2×10^4
N		239	239	239	239
Average	[0.32;0.34)	37.3	375.1	64.8	20.6×10^4
SD		6.4	37.5	15.9	5.6×10^4
N		160	160	160	160
Average	[0.34;0.37)	34.0	387.9	58.6	19.3×10^4
SD		6.0	54.4	27.2	8.6×10^4
N		149	149	149	149
Average	[0.37;0.42)	32.6	406.2	44.2	20.3×10^4
SD		8.3	50.3	18.2	11.4×10^4
N		164	164	164	164

and N.F. Ness) when available and to Exp.2 (Neubauer) otherwise. A subset corresponding to the HELIOS spacecraft passages between 0.29 and 0.47 AU has been selected (Diego et al., 2013). The IMF components (B_X, B_Y, and B_Z) are expressed in the solar ecliptic coordinate system. The SW parameters have been observed in the following intervals: 220 km/s _x0003C; V < 900 km/s; 2.0 nT < $|B|$ < 100 nT; 0.5 cm^{-3} < D < 300 cm^{-3}; 1.4×10^4 K < T < 1.1×10^6 K. In addition, the global averages (AV) and the corresponding SDs have been computed, obtaining V_{AV} = 417.6 km/s (SD_V = 120.6 km/s), $|B|_{AV}$ = 33.7 nT (SD_B = 9.9 nT), D_{AV} = 68.9 cm^{-3} (SD_D = 47.5 cm^{-3}), and T_{AV} = 24.3×10^4 K ($SD_T = 16.3 \times 10^4$ K).

In order to better characterize the SW parameters, we computed the average values for the SW background (hereafter unperturbed: UNP) as a reference level between 0.29 and 0.47 AU. For evaluating UNP parameters, we neglected intervals showing both long-term (lasting days) and short-term (lasting few hours) variations considering intervals without variations greater than 10% for, at least, 24 hr. The results obtained are reported in Table 1. The subset has the following average values: V_{UNP} = 384.2 km/s (SD_V = 50.7 km/s), B_{UNP} = 37.3 nT (SD_B = 7.7 nT), D_{UNP} = 60.4 cm^{-3} (SD_D = 23.5 cm^{-3}), and T_{UNP} = 19. 8×10^4 K ($SD_T = 9.8 \times 10^4$ K). Despite that the data distributions are not exactly Gaussian, we reported the SDs in order to have a rough measure of the range of variability of each parameter. Even if the unperturbed averages are generally lower than the global averages, as expected, it is worth noting that for unperturbed $|B|$ we found the opposite behavior, showing a greater value. A possible reason can be addressed to the evaluation of the SW_{UNP} averaged parameters that has been performed considering four radial distances. The analyzed data set shows, incidentally, that the majority of number of hours of SW_{UNP} (34%) was available at radial distances in the range 0.29–0.32 AU, (i.e., closer to the Sun). This peculiar radial occurrence of unperturbed values in Helios data set might have biased the computation of $|B|_{UNP}$ toward higher values. On the other hand, D_{UNP} is not greater than the global average. Such different behavior could be addressed to the peculiar features of some SW structures that are not considered in the unperturbed data set. In fact, global averages include also SW structures (e.g., the NCDEs described in the following) with IMF lower than the unperturbed observed at shorter distance from the Sun, but with very high density level, giving rise to an opposite behavior of B_{UNP} and D_{UNP} when compared to global averages.

It is furthermore interesting to note that V_{UNP} is considerably greater than the minima observed in V global range (i.e., 220 km/s), since some low speed streams, not considered as unperturbed, could have very low velocities (Sanchez-Diaz et al., 2016).

No decrease with the radial distance has been detected for unperturbed T, as shown in Table 1.

A more detailed characterization of the SW condition at Mercury's orbit was made for three types of interplanetary structures: (i) (HSSs), (ii) MCs, and (iii) NCDEs, as described in the following sections.

Table 2
High Speed Stream Events List

No.	Date	hr	SC	S-dist (AU)	$V_{\text{pre-increase}}$	V_{HSS} (km/s)	D_{HSS} (cm^{-3})	T_{HSS} (10^4 K)	$\lvert B\rvert_{\text{HSS}}$ (nT)	Polarity	Δt (hr)
1	13/03/1975	12	H1	0.31	344	602	34	43.7	41	+	84
2	20/03/1975	20	H1	0.33	321	517	16	28.8	39	+	50
3	11/09/1975	10	H1	0.35	316	617	25	37.9	31	+	89
4	14/03/1976	8	H1	0.31	426	581	24	35.0	24	−	183
5	28/03/1976	7	H1	0.31	390	509	53	43.1	41	+	65
6	05/04/1976	15	H1	0.35	476	535	37	37.6	24	−	136
7	04/10/1976	12	H1	0.31	387	467	39	36.6	39	−	80
8	05/04/1977	20	H1	0.35	461	578	34	35.8	34	+	124
9	15/10/1977	11	H1	0.31	440	555	41	43.1	36	+	156
10	06/11/1978	20	H1	0.33	307	527	34	41.1	41	−	92
11	06/05/1979	7	H1	0.31	360	455	48	24.8	47	−	244
12	12/04/1976	18	H2	0.30	409	706	29	52.9	42	−	165
13	02/05/1977	4	H2	0.35	325	522	39	38.1	27	−	94
14	19/04/1978	2	H2	0.36	508	542	27	30.2	32	−	67

Note. The second and third columns show the date and the first hour after the SI; the fourth and fifth columns display the SC label and its heliocentric distance; from the sixth to the ninth column we report the hourly averages of the SW parameters over the whole event (not including the stream interface for clearer results as already performed by Schwenn, 1990); the tenth column shows the IMF polarity; the last column display the number of hours (Δt) before the SW velocity returns to their preincrease value, if the behavior of D, $|B|$, and its components remain constant. Dates are formatted as DD/MM/YYYY.

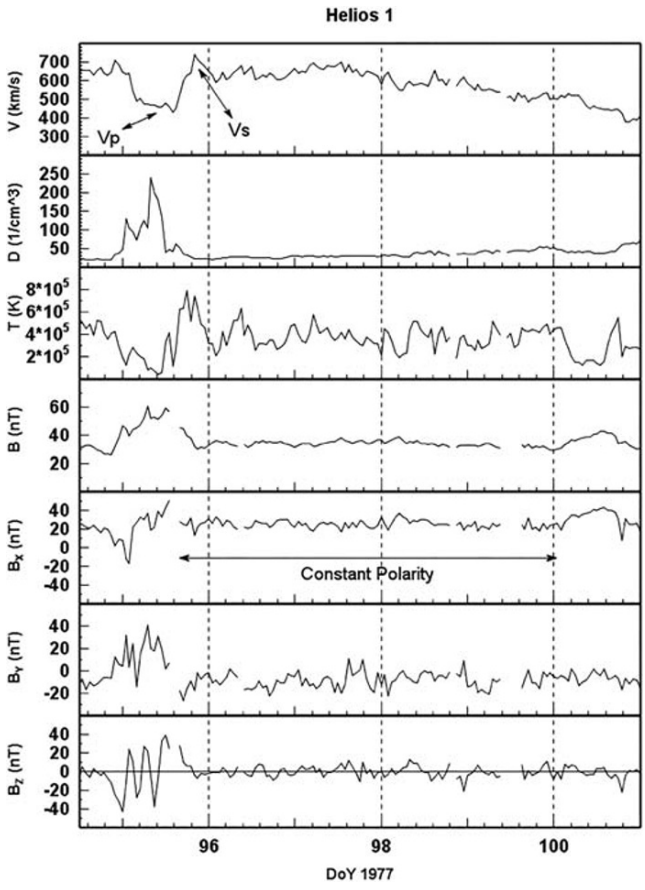

Figure 1. Helios 1 data for April 1977. HSSs are identified, from doy 95 up to doy 101.

2.1. HSS

The HSS identification was based on past findings about the stream nature (e.g., Diego et al., 2005; Gosling et al., 1978; Smith & Wolfe, 1979), namely, the stream interface (SI) is determined as a sudden enhancement of both B and D just before the increase in V and a concomitant lower $|B|$ and D values after the SI; only positive variation greater than 100 km/s between V and Vp (preincrease speed determined over the previous interval just before the SI) has been considered; the slow return of V to ambient conditions in several days (often more than 3 days); low values of $|B_Z|$ and a constant magnetic field polarity in the ecliptic plane for the whole stream duration (e.g., Iucci et al., 1979). The events selection has been performed by evaluating the 3-hr running averaged data variations in the time interval between the maximum values and the preincrease values. We found 14 HSS events (Table 2). Figure 1 shows an example (Event No. 8 in Table 2) of HSS, identified in April 1977. An increase of more than 200 km/s in V, after the D increase at the SI, is detected. High T values are observed, B_Z is close to 0, and both B_X and B_Y are nearly constant showing a defined magnetic field orientation. Furthermore, the behavior of the SW parameters for the selected HSSs allows to exclude transient phenomena such as shocks or interplanetary coronal mass ejections (ICMEs).

2.2. NCDEs

In order to select NCDE events, we considered a subset of CMEs characterized by a strong plasma density increase not induced by streams interaction but mostly by coronal filament disruptions (Gosling et al., 1977). In addition, to focus attention on independent SW structures, we choose to exclude from our analysis large density enhancements associated with CIRs/SIRs (acronyms for Corotating Interaction Region and Stream Interaction Region respectively). Thus, we mainly looked for the following SW features: High D when V is almost constant (or vary very gradually, i.e., ~100 km/s per day); low T, inversely varying with D; and IMF nearly constant at very low values. In addition, we required the D enhancement to be more than 2 times higher than the preincrease value

Table 3
Noncompressive Density Enhancement Events List

No.	Date	hr	SC	S-dist (AU)	Dp (cm^{-3})	D_{NCDE} (cm^{-3})	V_{NCDE} (km/s)	T_{NCDE} (10^4K)	$\|B\|_{NCDE}$ (nT)	Δt (hr)
1	11/03/1975	8	H1	0.32	89	168	269	10.1	30	14
2	18/09/1975	23	H1	0.31	62	154	285	11.0	25	95
3	23/03/1975	23	H1	0.34	43	169	363	6.6	22	15
4	27/03/1976	21	H1	0.31	36	191	394	12.1	26	22
5	01/04/1976	14	H1	0.33	80	140	325	14.0	25	48
6	04/10/1976	15	H1	0.31	100	179	383	18.6	28	12
7	13/04/1977	11	H1	0.31	55	163	311	9.5	25	19
8	22/10/1977	12	H1	0.31	47	117	332	12.6	25	97
9	18/10/1976	23	H2	0.29	47	229	337	7.5	17	22
10	17/04/1977	5	H2	0.32	120	146	338	9.6	32	31
11	02/05/1978	12	H2	0.3	59	123	365	21.6	40	70
12	01/11/1978	12	H2	0.29	122	163	323	13.3	51	22

Note. The second and third columns show the date and the onset of the event; the fourth and fifth columns display the SC label and its heliocentric distance; the sixth column shows the preincreased value; from the seventh to the tenth column we report the hourly averages of the SW parameters over the whole event; the last column displays the number of hours (Δt) before the SW velocity returns to their preincrease value, unless any variation occur in the other parameters. Dates are formatted as DD/MM/YYYY.

(Dp) and lasting for at least 12 hr. We identified 12 NCDE events, listed in Table 3. Figure 2 shows an example for the NCDE of 4 October 1976 (Event No. 6 in Table 3): V, T, $|B|$, and B_Z are very low, while the density increases of 195%. No clear polarity is expected to be identified in B_X and B_Y.

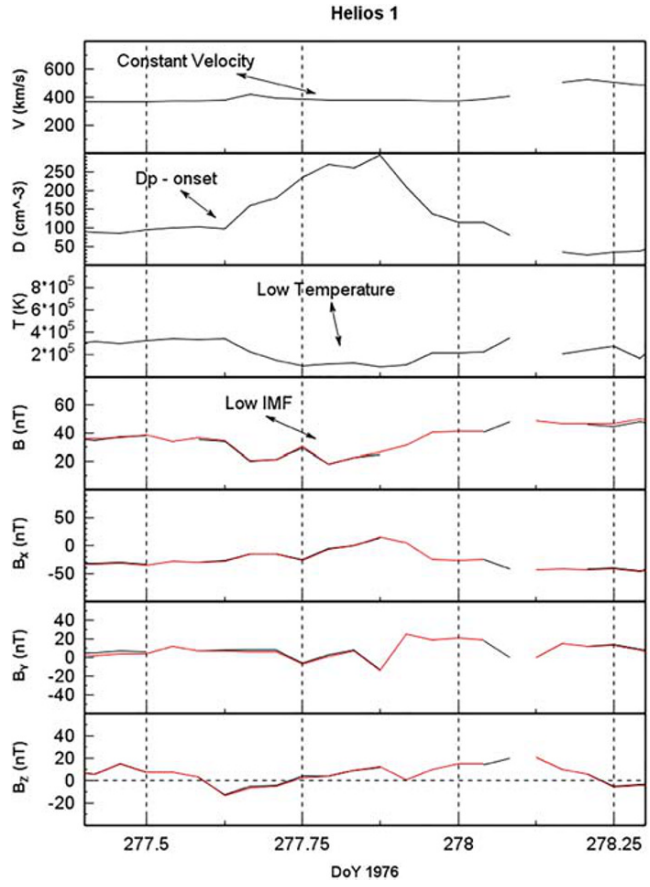

Figure 2. Helios 1 data for October 1976. A NCDE is identified at doy 277.

2.3. MCs

The MC were identified by using the results by Klein and Burlaga (1982), namely, enhanced $|B|$, almost planar rotation of B components, and low T. According to Burlaga et al. (1981), we focused our attention to B_Z variations as reports in Table 4. So, we first selected data from Bothmer and Schwenn (1998), Blanco et al. (2013), and Cane et al. (1997) catalogs for H1 or H2 located between 0.29 and 0.47 AU. In addition to these, other events having high $|B|$ and B_Z variations have been included. Increase amplitudes of B are detected as the difference between the maximum value during the MC and the preincrease values (B_{MC} and Bp in Table 4).

Figure 3 displays a slight increase of $|B|$ (starting at the beginning of doy 64, 1975), while V and T are very low. B_Z start its typical variations, assuming negative (−26 nT) and positive (40 nT) values during the doy 64, 1976.

3. SW Parameter Analysis for the Identified Structures

Figure 4 (upper panel) shows the number of detected structures of SW parameters at every passage of HELIOS satellites between 0.29 and 0.47 AU. The obtained occurrence of different classes of structures are in good agreement with space climate variability knowledge in terms of occurrences of various SW structures near the Earth (Cliver et al., 1996). In fact, the relative percentage of each class depends on the phase and amplitude of solar activity cycle. Note that the low occurrence of SW structures near the maximum phase in Figure 4 (upper panel) is mainly due to the great lack of HELIOS data of that period. In fact, the HELIOS data coverage is about 50% in late 1979 and 1980 and about 20% in 1981 (as shown in lower panel).

In order to outline interplanetary medium conditions for different SW regimes, the data distributions have been computed for each class of structures. SW parameters distributions are reported in Figures 5a, 6a, and 7a, where HSSs (red histograms), NCDEs (blue histograms), and

Table 4
Magnetic Cloud Events List

No.	Start date	hr	SC	S-dist (AU)	Bp (nT)	$\lvert B\rvert_{MC}$ (nT)	V_{MC} (km/s)	D_{MC} (cm^{-3})	T_{MC} (10^4 K)	B_Z max excursion (nT)		Δt (hr)
1[a,b]	04/03/1975	15	H1	0.38	16	49	471	61	9.8	−26	40	14
2	19/03/1975	6	H1	0.32	21	46	368	88	12.1	−25	40	27
3[b]	27/03/1976	5	H1	0.32	28	52	435	40	26.8	50	−7	16
4[b]	12/05/1978	5	H1	0.41	25	53	713	68	36.3	−81	28	15
5[a,b]	18/10/1978	19	H1	0.47	24	46	504	51	14.2	−57	58	25
6[a,b]	28/05/1979	21	H1	0.43	18	74	508	69	9.1	−85	30	16
7[a,b]	31/03/1976	7	H2	0.47	20	42	451	29	13.4	23	−45	21
8	26/10/1977	15	H2	0.29	16	38	282	155	14.5	−31	34	25
9[a,b]	24/04/1978	12	H2	0.31	33	68	398	108	8.5	−82	7	18
10[a,b]	09/05/1979	4	H2	0.29	41	123	607	92	28.3	−57	123	15

Note. MC-V, MC-D, MC-T, and MC-B, are average values, and B_Z excursion are maxima of hourly data during each event. Dates are formatted as DD/MM/YYYY.
[a]Events already identified by Bothmer et al. [b]Events already identified by Blanco et al.

MCs (green histograms) are displayed together with an equivalent selection performed at 1 AU (Figures 5b, 6b, and 7b) as described in section 4. It is interesting to note that distributions are noticeably different for the identified classes, both in shape and average values. Average values and SDs reported in Table 5 have been calculated either for global data set (6,818 hourly values) and for each class of SW structures (1,629 hr for HSSs, 467 hr for NCDEs, and 192 hr for MCs, as the sum of their durations reported in the last column of Tables 2–4, respectively).

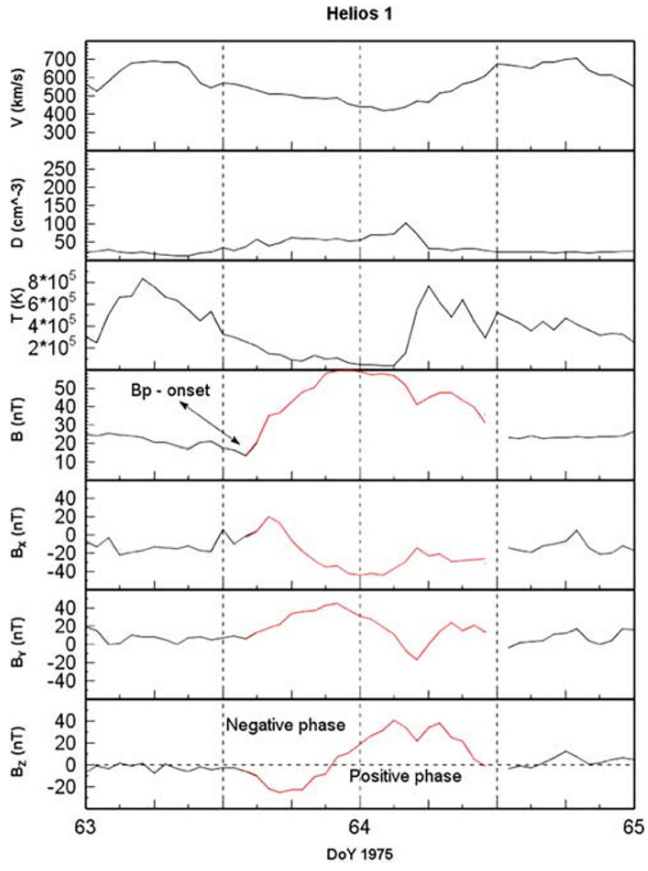

Figure 3. Helios 1 data for March 1975. A MC is identified, from doy 63 up to doy 64.

The comparison between global distribution (black staircase) and single class distributions (colored histograms) allows to understand the role of various SW regimes with respect to global features. Such comparison is expressed as the percentage of each average with respect to the global one, for all the considered SW parameters.

The velocity, as expected, shows higher values for HSSs (+31%) and a moderate increase for MCs (+10%). The V reduction of −20% for NCDEs can be addressed to their identification method requiring density enhancements without interactions with fast SW.

D shows large differences among the regimes, being the global mean equal to 68.9 that reduces of about 50% (34.8 cm^{-3}) for HSSs, while increases of 13% (78.2 cm^{-3}) and 121% (152.6 cm^{-3}) for MCs and NCDEs, respectively.

$|B|$ shows peculiar features being HSSs values higher with respect to transient NCDEs. In fact, we found +5% for HSSs, +67% for MCs, and −17% for NCDEs. This effect is even more evident if evaluated on B_X (Figure 6, left panel), showing an increase of $\simeq$ +15% for HSSs, probably due to lower values of Parker spiral angle (about −14° on average for HSSs) with respect to both transient NCDEs and MCs (about −20° and −22°, respectively, as shown in Figure 7). On the other hand, no remarkable differences were found on the averages of both B_Y and B_Z among the three classes of SW structures (Figure 6, middle and right panels, respectively), except for the larger distributions of MCs, which is probably due to the IMF rotations that produces a larger range of values.

Also, T has a high variability with respect to the global average showing an increase of 54% for HSSs and a decrease of −31% and −50% for MCs and for NCDEs, respectively. Note that, at Mercury's orbit, HSSs are the hottest plasma population, as well as at 1 AU (see Figure 7—central panels). Such results are phenomenologically consistent with THE model of SW acceleration proposed by Leer et al. (1982), in which

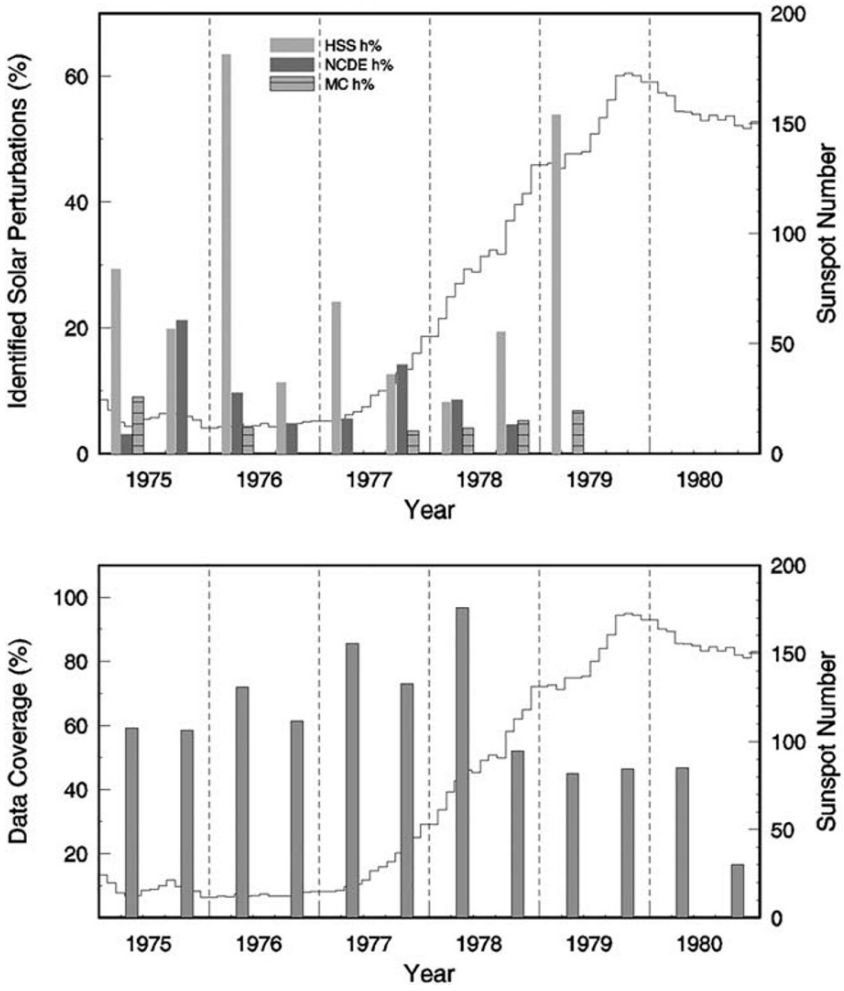

Figure 4. Solar wind structures occurrence displayed as percentage of the total observed period for the three different classes of perturbations (upper panel). In the lower panel are reported the effective data coverage for each passage in the range between 0.3 and 0.47 AU.

magnetohydrodynamic (MHD) waves play a major role in accelerating the plasma and heating the protons. In fact, as showed in Lopez (1987), there exists a direct relation between SW temperature and speed, for which high V are expected to produce high T, except inside ICMEs.

SW dynamic pressure (Figure 7, left panels) does not show remarkable differences among various structures, probably due to the alternating increases of D and V among the various structures. It is noteworthy that observed differences among average values of the SW structures are larger than the variability induced by the radial decrease between 0.29 and 0.47 (Slavin & Holzer, 1981). The map in the upper panel of Figure 8 shows the probability density of the entire Helios data set used relative to the SW velocity versus density. The probability density has been estimated constructing bivariate histograms and using a kernel density estimator (e.g., Martinez & Martinez, 2002) with the following bin sizes: plasma density, 0.3 cm^{-3}; velocity, 2 km/s; B_X and B_Z, 0.5 nT. Parameters clearly appear to be anticorrelated, with the higher velocity occurring at lower density and vice versa. The lower panel of Figure 8 displays the probability between B_X and B_Z showing that the average B_Z is around 0, while B_X peaks is at about +30 and −30 nT, as expected from the two different polarity (outward and inward) already shown in Figure 6a. These results agree with Sarantos & Slavin, 2009 where MESSENGER data have been used to obtain the same probability distributions for two separate data sets relevant to aphelion and perihelion of Mercury's radial distance from the Sun.

We repeated the same analysis also for the three subsets of HSS, MC, and NCDE. The results in Figure 9 are displayed in the same range of values in order to easily identify the probability peak position with respect to

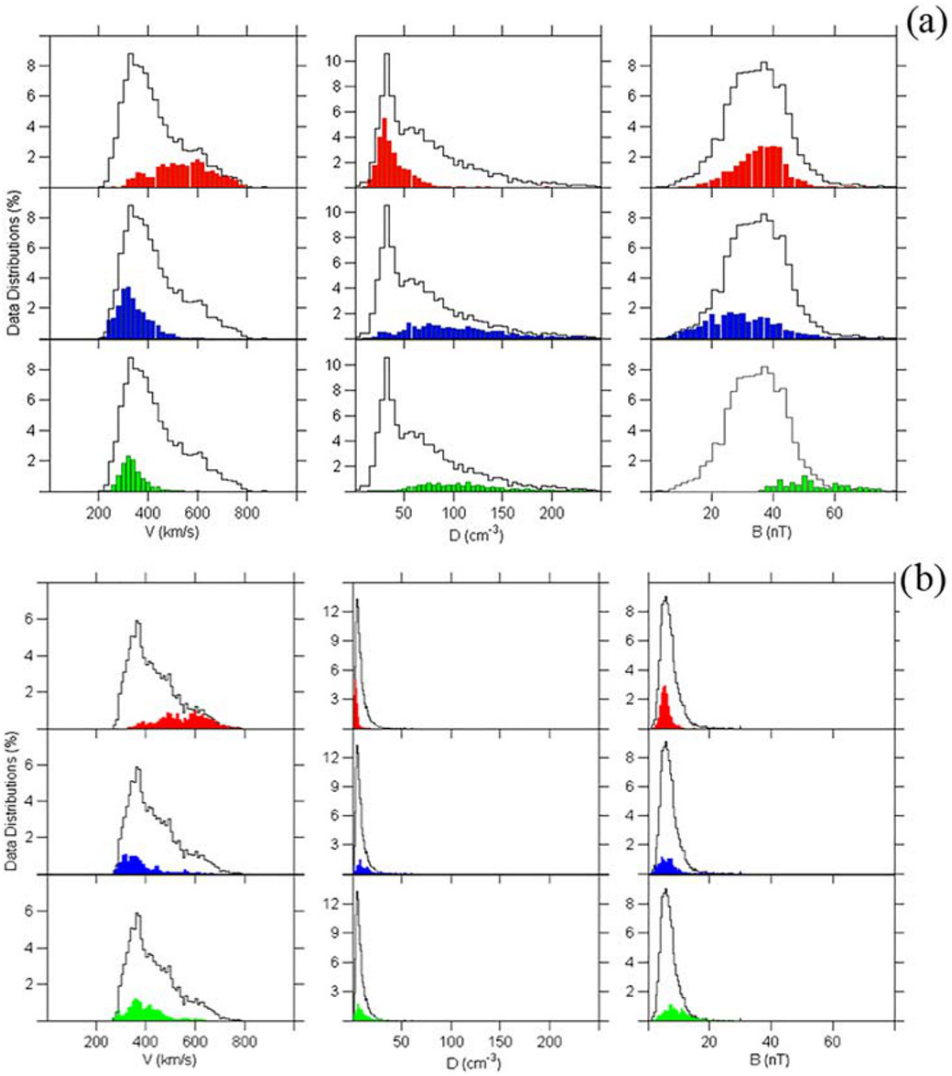

Figure 5. (a) SW velocity, density, and $|B|$. Helios data recorded at Mercury's orbit. White shape represents the entire data set, while colored ones represent HSSs (red), MCs (green), and NCDEs (blue). (b) SW velocity, density, and $|B|$. OMNI data recorded at Earth's orbit. White shape represents the entire data set, while colored ones represent HSSs (red), MCs (green), and NCDEs (blue).

Figure 8, while the color scale has been adjusted to better highlight the different position of the peaks. Results can be summarized as follows:

- HSSs (Figure 9, left) are characterized by lower D (upper panel) coupled with higher V (peak at about 600 km/s); B_X (lower panel) peaking at values of $\pm$30 nT with a high probability, coupled with B_Z peaking at ~0, as expected (DiBraccio et al., 2015, and reference therein).
- MCs shows the most probable speed values between 400 and 550 km/s with quite low density still comparable to that of HSSs. It is also present a higher density/lower speed tail. The IMF shows a more diffuse probability for both B_X and B_Z. In particular, both components distributions are enlarged by the typical rotation of B in the cloud.
- NCDEs have the lowest velocity with the highest density. The peculiar occurrence of positive B_X peak is probably due to the small data set identified for this kind of perturbation.

Figure 10 presents the Alfvénic Mach number, (M_a) as a function of both the sonic Mach number (M_S, left panels) and the SW pressure, (P_{SW}, right panels). Upper panels show the probability density function for the

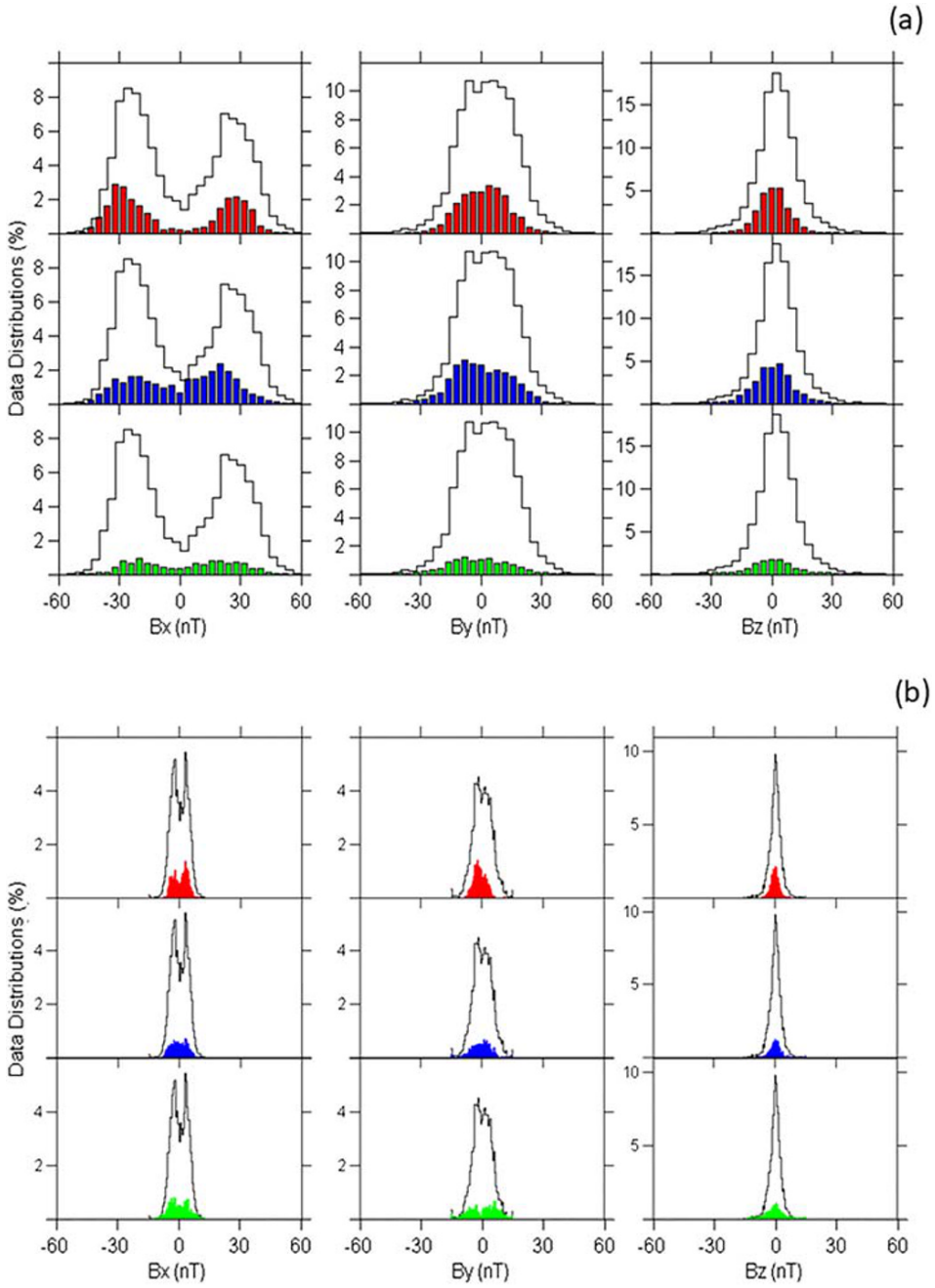

Figure 6. (a) IMF components data distributions. Helios data recorded at Mercury's orbit. White shape represents the entire data set, while colored ones represent HSSs (red), MCs (green), and NCDEs (blue). (b) IMF components data distributions. OMNI data recorded at Earth's orbit. White shape represents the entire data set, while colored ones represent HSSs (red), MCs (green), and NCDEs (blue).

total data set. We found that the typical plasma conditions at Mercury's orbit are the same as in Sarantos and Slavin (2009), corresponding to $2 < M_a < 6$, $3 < M_S < 7$, 4 nPa $< P_{SW} <$ 27 nPa, $0.5 < \beta < 2.2$, and 32 nT $< |B| <$ 55 nT. Lower panels show the probability density functions for the HSS, MC, and NCDE data sets, respectively. We found that the typical plasma conditions for the HSSs are characterized by a lower M_a ($1.8 < M_a < 4$), as expected for the concurring contribution of a higher radial IMF (B_X) and lower density (see Table 5). In addition, the M_S range (2 to 11) can reasonably addicted to the high T in HSSs.

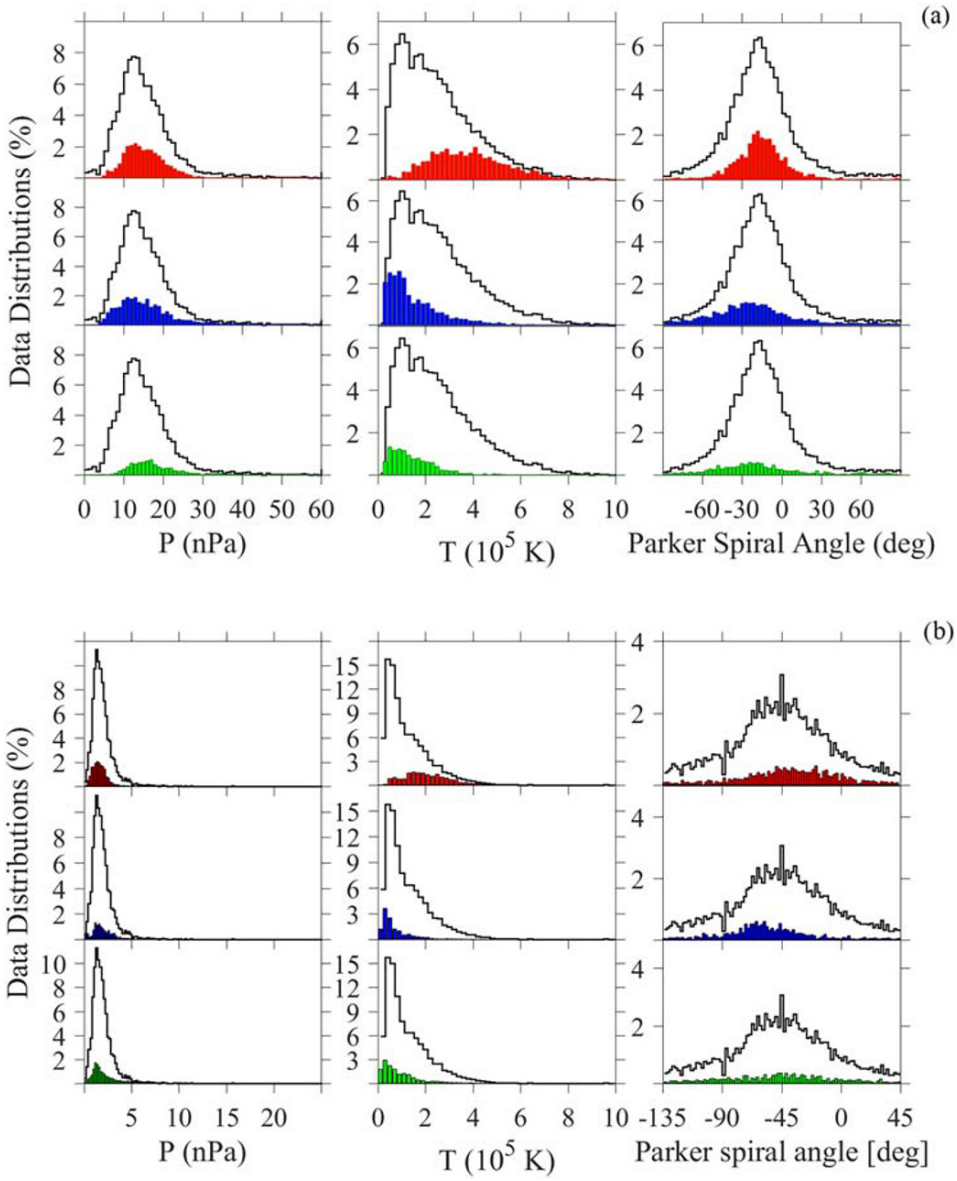

Figure 7. (a) SW pressure, temperature, and IMF spiral angle distributions. Helios data recorded at Mercury's orbit. White shape represents the entire data set, while colored ones represent HSSs (red), MCs (green), and NCDEs (blue). IMF spiral angle is always considered outward (being computed as arctan $|B_Y|/|B_X|$). (b) SW pressure, temperature, and IMF spiral angle distributions. OMNI data recorded at Earth's orbit. White shape represents the entire data set, while colored ones represent HSSs (red), MCs (green), and NCDEs (blue). IMF spiral angle is always considered outward (being computed as arctan $|B_Y|/|B_X|$).

MCs most probable plasma conditions are characterized by M_a that extend between 1.6 and 5. In addition, we did not find M_a greater than 10. On the other hand, sonic Mach number and dynamic pressure are in the range $1.5 < M_S < 16$ and $0.5\ \text{nPa} < P_{SW} < 37\ \text{nPa}$. Such M_a, M_S, and P_{SW} values are due to higher IMF, lower temperature, and higher density conditions (see Table 5), which are typical of the leading part of MCs (Sarantos & Slavin, 2009).

NCDE most probable plasma conditions are $2 < M_a < 14$, $2 < M_S < 10$, $10\ \text{nPa} < P_{SW} < 35\ \text{nPa}$. This range values are due to the low IMF, to the low temperature, and huge density values (see Table 5). Interestingly, we did not observe M_S greater than ≈14. This is probably due to the low SW speed values of NCDE.

Table 5
Mean Values of Interplanetary Magnetic Field Components and Solar Wind Dynamic Pressure for HSSs, MCs, and NCDEs at Mercury's Orbit

	$\|B\|$ (nT)	$B_{X,\mathrm{Pos}}$ (nT)	$B_{X,\mathrm{Neg}}$ (nT)	B_Y (nT)	B_Z (nT)	D (cm^{-3})	T (10^4 K)	V (km/s)	β
Total mean	33.7	23.8	−24.4	0.7	0.3	68.9	24.3	417.6	0.6
Total_std	9.9	10.8	9.8	13.6	10.7	47.5	16.3	120.6	0.76
HSSs mean	35.4	28.2	−27.1	2.2	0.7	34.8	37.4	548.9	0.45
HSSs_std	8.9	7.6	10.2	10.8	7.4	12.6	14.7	117.9	0.67
MCs mean	56.3	23.4	−29.2	7.2	−1.1	78.2	16.7	459.6	0.21
MCs_std	26.8	14.5	20.9	32.3	35	55.1	13.3	123.2	0.45
NCDEs mean	27.9	17.7	−17.5	−3.5	−2.3	152.6	12.3	325.8	1.31
NCDEs_std	10.6	9	9.7	12.2	12.5	52.3	6.9	40.8	1.14

Note. Data from Helios satellites.

4. Radial Behavior of Different SW Regimes

The SW values at Mercury's orbit, reported in Table 5, have been compared with those detected at Earth's orbit over the same observing period in order to outline their radial evolution as a function of the different structures. For this purpose, 9 HSSs, 10 NCDEs, and 13 MCs have been identified by using OMNI data for the same period and the same method adopted for the selection on Helios data. The statistical distributions performed on the data sets of each parameter allowed to verify some aspects of their radial dependence (e.g., Mariani et al., 1979). Average values relevant to the data sets selected at 1 AU are reported in Table 6. Characteristic radial variations of different SW regimes are outlined from the histograms in Figures 5–7 where the number of bins is the same for both Mercury's (Figures 5a, 6a, and 7a) and Earth's case (Figures 5b, 6b, and 7b), while the bin sizes have been consequently adjusted for each range extensions. Radial variations of SW parameters are expressed as ratio between HELIOS and OMNI average distribution (Table 7) values (H/O) for global data set and single structure's subset as well.

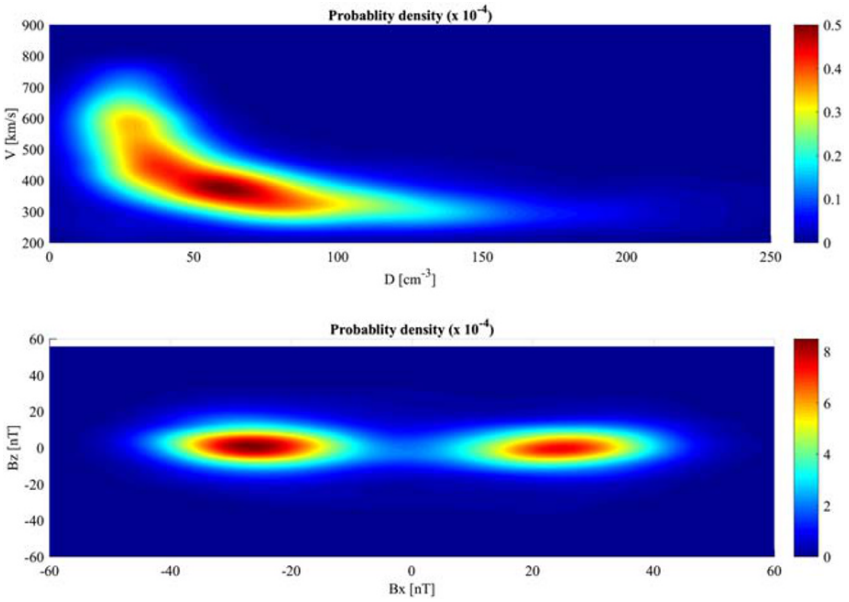

Figure 8. The upper panel shows the probability density of the entire Helios data set used relevant to the SW velocity versus density. Parameters clearly appear to be anticorrelated, with the higher velocity occurring at lower density and vice versa. The lower panel displays the probability B_X and B_Z showing that the average B_Z is around 0, while B_X peaks can be identified at about +30 and −30 nT as expected from the two different IMF directions.

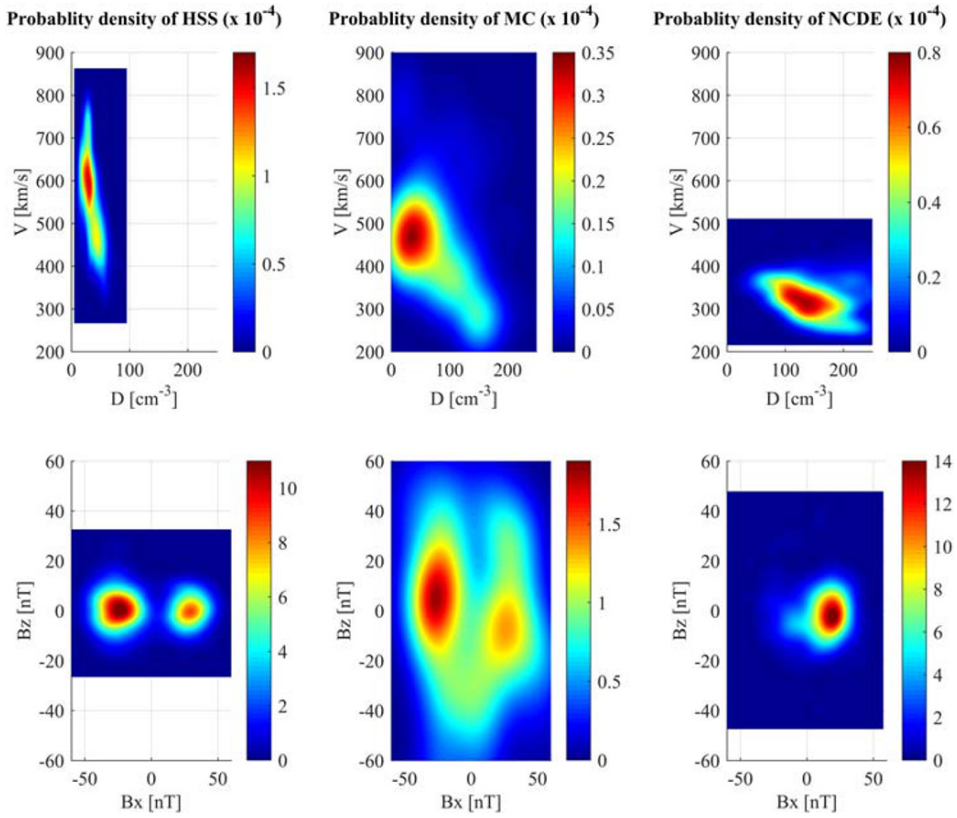

Figure 9. Probability density as in Figure 8 for the three subsets of HSS, MC, and NCDE. Results are displayed in the same range of values in order to easily identify the probability peak position with respect to that of Figure 8, while the color scale has been adjusted to better highlight the different position of the peaks.

4.1. HSS

For the HSSs, we made a comparison between HELIOS and OMNI recorded in the same periods by assuming that, under the influence of the same solar structures, the SW variations could have similar intensity and duration. In addition, due to CH (the sources of HSSs) persistency in time, shape, and position on the Sun's disk, we can reasonably consider that Helios and OMNI were connected with the same solar source at different times.

As expected by r^{-2} power law (Richardson & Cane, 2010), the density decreases of about 10 times from 0.29 to 1 AU (Figures 5a and 5b, middle panels).

Figures 6a and 6b shows that on average the IMF is about 7 times greater at Mercury. In fact, H/O (B_{HSS}) = 7.3 (see Table 7) is in good agreement with the results obtained by Khabarova and Obridko (2012). Moreover, the ratio H/O ($B_{X,HSS}$) = 9.2 evaluated for the radial IMF component confirms the expected radial decrease of r^{-2}. Finally, although Mariani et al. (1979) described an almost inverse ($\simeq 1/r$) radial trend for B_Y (about H/O $\simeq$ 3), we observed for HSSs cases a higher decrease, characterized by a ratio H/O ($B_{Y,HSS}$) > 4 (Figures 6a and 6b, central panels). This difference could be due to the contributions of Alfvénic ultralow frequency (ULF) waves, mainly oscillating on *YZ* geocentric solar ecliptic (GSE) plane (Diego et al., 2005), that may enlarge the range at Mercury's orbit (Korth et al., 2011). Such effect is particularly important for small spiral angles (e.g., for HSSs).

In addition, we found that global range of temperature is about 2 times greater around Mercury's orbit (Figures 7a and 7b, central panels), confirming that HSSs are the structures with the hottest plasma. These results are in good agreement with Slavin and Holzer (1981) and Scudder (2015). Finally, values of β (last column in Tables 5 and 6) shows that HSSs are characterized by $\beta < 1$ (i.e., magnetic pressure is greater than plasma dynamic pressure) around Mercury's orbit.

Table 6
Mean Values of Interplanetary Magnetic Field Components and Solar Wind Dynamic Pressure for HSSs, MCs, and NCDEs at Earth's Orbit

	$\|B\|$ (nT)	$B_{X,\mathrm{Pos}}$ (nT)	$B_{X,\mathrm{Neg}}$ (nT)	B_Y (nT)	B_Z (nT)	D (cm^{-3})	T (10^4 K)	V (km/s)	β
Total[a]	6.7	3.4	−3.22	0.2	−0.03	7.5	11.8	427.6	0.86
Total_std[a]	3.1	2	2.1	4.7	2.9	5.6	10.5	97.4	0.74
HSSs[a]	5.6	3.3	−2.7	−1	−0.06	3.7	20.6	550.8	0.97
HSSs_std[a]	1.5	1.7	1.5	2.8	1.9	1.7	9.9	91.1	0.68
MCs[a,b]	15.5	3.9[a]	−3.7[a]	0.9[a]	−10.5[d]	6.6[e]	2.9	485	0.52
MCs_std[a,b]	5.9	2.6[a]	2.3[a]	6.7[a]	5.2[a]	0.3[e]	0.3	101	0.72
NCDEs[a,c]	5.6	3.2[a]	−3.1[a]	0.4[a]	0.2[a]	22.1	3.3	362	0.94
NCDEs_std[a,c]	2.2	1.9[a]	2.0[a]	4.5[a]	2.6[a]	6.4	1.4	42	0.88

[a]Data from this work. [b]Data from Echer et al. (1999). [c]Data from Gosling et al. (1977). [d]Bs instead of B_Z. [e]Data from Richardson and Cane (2010).

4.2. Noncompressive Density Events

NCDEs show a radial density decrease rate lower than the expected r^{-2} (Richardson & Cane, 2010). In fact, we found a density ratio H/O (D_{NCDE}) = 6.9, probably due to the NCDEs propriety of storing high plasma density.

The IMF B_X is characterized by a radial variation that differs from the expected decrease rate of r^{-2}. In fact, Figures 6a and 6b and Table 7 show that, on average, the IMF is 5 times greater at Mercury as expected from a decrease law of about $r^{-3/2}$ (Mariani et al., 1978) but we found H/O ($B_{X,\mathrm{NCDE}}$) = 5.5 and 5.6 (for positive and negative orientations, respectively) that is significantly lower than that of other SW structures and the global ratio.

For NCDE the T decrease does not follow the law $r^{-2/3}$ of global and HSSs, but its slope has a decrease law of about $r^{-3/2}$. Finally, values of β (last column in Tables 5 and 6) shows that NCDEs are characterized by $\beta > 1$ around Mercury's orbit.

4.3. MC

MCs show a radial density decrease rate quite in agreement with the expected r^{-2} (Richardson & Cane, 2010). In fact, we found a density ratio H/O (D_{MC}) = 11.8.

Figures 6a and 6b show that on average the IMF is about 4 times greater at Mercury. In fact, H/O (B_{MC}) = 3.6 (see Table 7) are in good agreement with the results obtained by Khabarova and Obridko (2012). Moreover, the ratio H/O ($B_{X,\mathrm{HSS}}$) = 8.6 evaluated for the radial IMF component confirms the expected radial decrease of r^{-2}. Finally, although Mariani et al. (1979) described an almost inverse ($\simeq 1/r$) radial trend for B_Y (about H/O $\simeq$ 3), we observed (Figures 6a and 6b, central panels) for MCs cases a higher decrease, characterized by a ratio H/O ($B_{Y,\mathrm{HSS}}$) = 8.1. This result suggests that, for MC, the B_Y follows a radial decrease of r^{-2}.

In addition, we found that global range of temperature around Mercury's orbit (Figures 7a and 7b, central panels), is similar to the Earth's orbit.

These outcomes are in agreement with Liu et al. (2005, 2006), who find comparable results for the radial evolution of SW density, SW temperature, and IMF components.

Table 7
Ratio Between Interplanetary Medium Parameters at Mercury's and Earth's Orbit for Different SW Regimes

	$H_{\|B\|}/O_{\|B\|}$	$H_{BX}/O_{BX\mathrm{positive}}$	$H_{BX}/O_{BX\mathrm{negative}}$	H_{BY}/O_{BY}	H_{BZ}/O_{BZ}	H_D/O_D	H_T/O_T	H_V/O_V	H_β/O_β
Total	5.0	7.0	7.6	3.5	n.a.	9.2	2.0	1.0	0.69
HSSs	6.3	8.5	10.0	−2.2	n.a.	9.4	1.8	1.0	0.46
MCs	3.6	6.0	7.9	8.0	n.a.	11.8	5.8	0.9	0.40
NCDEs	5.0	5.5	5.6	−8.7	n.a.	6.9	3.6	0.9	1.39

Note. Ratio between B_Z values is considered not applicable (n.a.) because values close to 0 of averages produce not reasonable results.

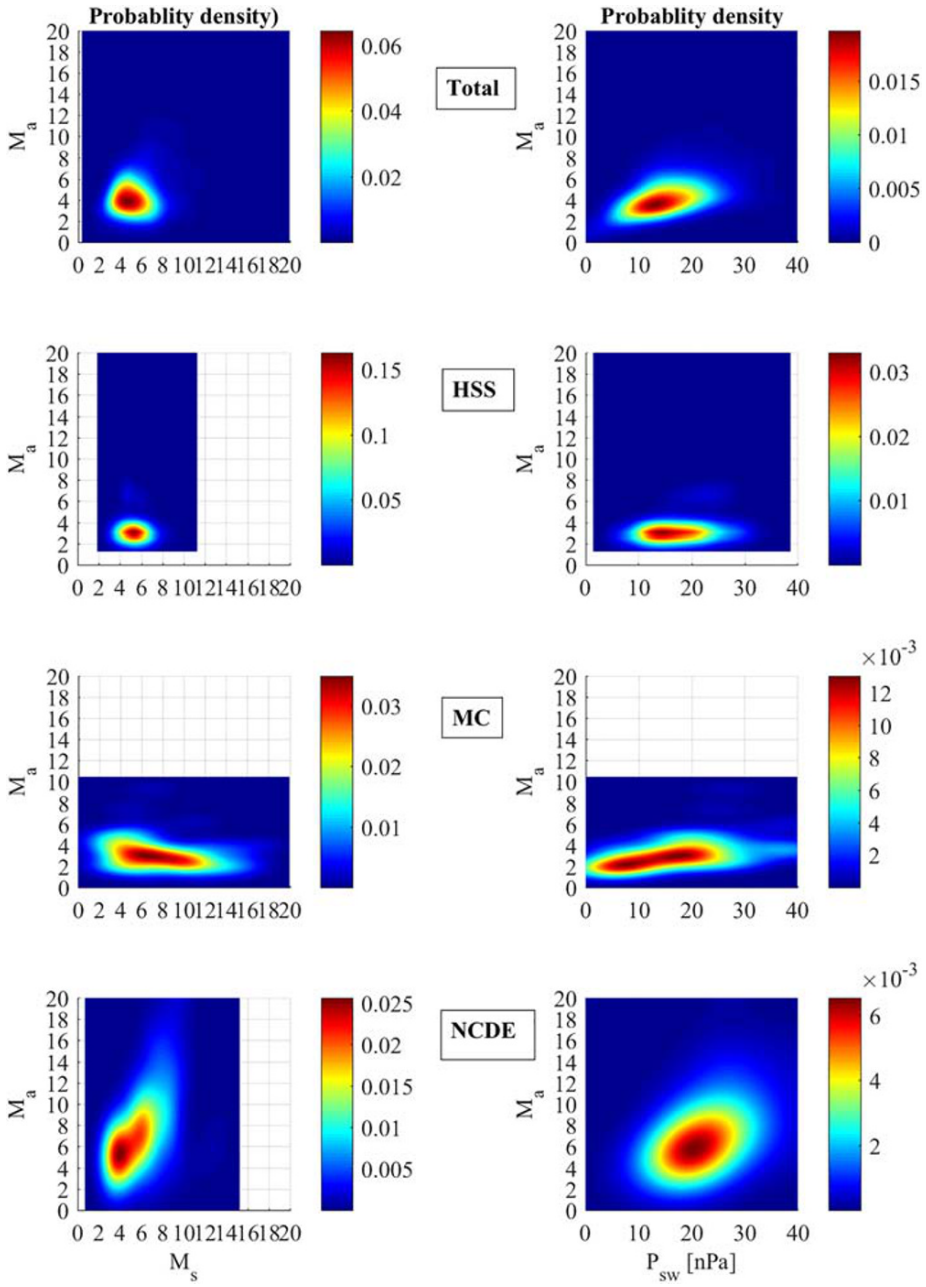

Figure 10. Probability density as in Figure 9 relevant to Alfvénic Mach number (M_a) versus sound Mach number (M_S) and dynamic pressure (PSW) for the three subsets of HSS, MC, and NCDE. As in Figure 9, results are displayed in the same range of values in order to easily identify the probability peak position but with different color scale.

Finally, as for HSS, values of β (last column in Tables 5 and 6 show that MCs are characterized by $\beta < 1$ (i.e., magnetic pressure is greater than plasma dynamic pressure) around Mercury's orbit. This result is in agreement with the Kumar and Rust (1996) model, who estimates $\beta = 0.52$ at 0.3 AU.

5. Summary and Conclusion

A comprehensive and detailed characterization of the SW conditions at Mercury's orbit (i.e., between 0.29 and 0.47 AU) has been performed by using hourly data of Helios 1 and 2 to identify occurrences and features

of three types of SW structures, namely, HSSs, NCDEs, and MCs, as described in section 2 (event list in Tables 2–4 respectively).

The results of this work aim to add information on the following topics:

- Space climatology (e.g., occurrences, characteristics, and durations of SW structures traveling in the interplanetary space)
- Radial variations for the various SW structures
- Constraints for modeling of the Hermean magnetosphere and of the propagation and expansion of interplanetary transients.

The present analysis shows the following:

i. SW regimes separation could be very useful for studies of interplanetary space conditions (space weather) and the effects on planetary magnetospheres. In addition, the analysis of the occurrence of various SW structure along the solar cycle improves the comprehension of the space climate along the solar cycles. The phase of solar cycle represents, by definition, the temporal evolution of sunspots number that is highly related to occurrence of transient structures. On the other hand, HSSs occurrence on the ecliptic plane is related to the presence of CH at low solar latitudes. This condition is mainly observed during descending and minima phases of solar cycles. Due to the random release of MCs and NCDEs, their occurrence rate reported in this work is not representative for the actual number of active regions on the Sun. Therefore, transient structures detected are only a fraction of that actually traveling in the interplanetary space. On the other hand, due to the long-lasting duration of CH that continuously generate fast SW, the HSSs are surely identified by space mission measurements (if orbiting at solar latitudes spanned by the CH).

ii. SW parameter values are expected to show variabilities induced by solar activity (time variation) and radial evolution (space variations). We want to point out that a sharp characterization of SW structures is able to explain the observed variability (i.e., global range of each parameter). The average values of SW parameters (reported in section 3) computed on each structure's data set are very different one to each other and from the unperturbed values (reported in Table 1). Moreover, their differences are largely greater than the expected radial variation of each parameter. Figures 5–7 show the position of each structure within the global distribution. Results of the characterization of SW structures detected at 0.29–0.47 AU are summarized in Table 5, whereas Figures 5–7, show the position of each structure within the global distribution. In addition, Figures 8 and 9 emphasize the different features among the structures and the comparison with and the global one.

In addition, Figures 5b, 6b, and 7 display results of a similar analysis performed at 1 AU on the same type of SW structures (but not on the same events). Our analyses confirm previous results about $|B|$ ratios between Helios and OMNI (H/O) that are in agreement with Burlaga (2001), who found a radial decrease in the range of 3–6. Our results show that MC's population is responsible for the lower decrease ($H/O_{MCs} = 3.6$) and HSSs are responsible for the higher decrease ($H/O_{HSSs} = 6.3$). Table 7 confirms that the radial variations of the global data set are quite different to that of the various SW regimes. Each one of the selected categories shows a peculiar discrepancy from the expected radial behavior deduced from the entire data set.

iii. Features of various SW structures at Mercury's orbit are reported in section 2 and in Tables 2–4 while Table 5 summarizes their average values. For HSSs is noteworthy the steep B_X variation that produces high values of radial IMF. As shown in Figures 5–7, we found that B_X presents global range of values 7 times greater than Earth's orbit (Figure 6b left panels). In fact, the computed ratio Helios/Omni ($B_{X,HSS}$) is 8.5 for positive and 10 for negative cases, respectively. Moreover, also the dynamic pressure is about 10 times greater at about 0.3 AU (Figure 7a, left column) respect 1 AU (Figure 7b, left column). This is due to its linear dependence from the SW density which is greater of about 9 times with respect to 1 AU.

NCDEs is characterized by the capability of retain high density at increasing distance, as well as the IMF for MCs. In general, we found that the IMF at Mercury's orbit, when separated in structures, shows smaller variations with respect to other parameters. For instance, during HSSs, $|B|$ values are almost equal to the transient ones.

In order to deduce the most probable SW conditions at Mercury's orbit, we have applied our results in the probability density maps of Figures 8 and 9. The global expectation is shown in Figure 8 where D and V are strongly anticorrelated, and IMF displays a clear separation from positive and negative orientation resulting in high B_X and low B_Z probability. The maps in Figure 9 show differences in the probability density among various structures. V-D probability map confirms the global anticorrelation, but the expected values are very different among them. On the other hand, $B_{X\text{-}Z}$ probability shapes show different behavior. In fact, HSS has a sharp separation between the two IMF B_X directions, while for MCs it tends to be reduced, until it disappears for NCDEs.

We finally want to underline that the probability densities give more precise indications when associated to a rigorous SW structures selection which are also associated to different occurrence rate and durations.

Lastly, we want to stress that the statistical analysis provided here is relevant the increasing phase of the solar cycle as well as the phase of the arrival of BepiColombo in 2025.

Data Availability Statement

The HELIOS hourly data have been retrieved from the following web pages (https://spdf.gsfc.nasa.gov/pub/data/helios/helios1/mag/, https://spdf.gsfc.nasa.gov/pub/data/helios/helios2/mag/, https://spdf.gsfc.nasa.gov/pub/data/helios/helios1/plasma/hour/, and https://spdf.gsfc.nasa.gov/pub/data/helios/helios2/plasma/hour/).

Acknowledgments

This paper has been partly supported by the Italian Space Agency (Contract ASI/INAF I/022/10/0) for the BC Mission. Authors want to thank the work package responsible Dr. Marisa Storini for supporting this work. M. Piersanti thanks the Italian Space Agency for the financial support under the contract ASI "LIMADOU scienza" n° 2016-16-H0.

References

Blanco, J. J., Hidalgo, M. A., Gómez-Herrero, R., Rodríguez-Pacheco, J., Heber, B., Wimmer-Schweingruber, R. F., & Martín, C. (2013). Energetic-particle-flux decreases related to magnetic cloud passages as observed by the Helios 1 and 2 spacecraft. *A&A*, *556*, A146. https://doi.org/10.1051/0004-6361/201321739

Bothmer, V., & Schwenn, R. (1998). The structure and origin of magnetic clouds in the solar wind. *Annales de Geophysique*, *16*(1), 1–24. https://doi.org/10.1007/PL00021390

Burlaga, L. (2001). Magnetic fields and plasmas in the inner heliosphere: Helios results. *Planetary and Space Science*, *49*, 1619–1627. https://doi.org/10.1016/S0032-0633(01)00098-8

Burlaga, L. F. (1996). Intermittent turbulence in the solar wind. *Journal of Geophysical Research*, *96*(A4), 5847–5851. https://doi.org/10.1029/91JA00087

Burlaga, L. F., Sittler, E., Mariani, F., & Schwenn, R. (1981). Magnetic loop behind an interplanetary shock: Voyager, Helios and IMP-8 observations. *Journal of Geophysical Research*, *86*(A8), 6673–6684. https://doi.org/10.1029/JA086iA08p06673

Cane, H. V., Wibberenz, G., & Richardson, I. G. (1997). Helios 1 and 2 observations of particle decreases, ejecta and magnetic clouds. *Journal of Geophysical Research*, *102*(A4), 7075–7086. https://doi.org/10.1029/97JA00149

Cliver, E. W., Boriakoff, V., & Bounar, K. H. (1996). The 22-year cycle of geomagnetic activity. *Journal of Geophysical Research*, *101*(A12), 27,091–27,109. https://doi.org/10.1029/96JA02037

DiBraccio, G. A., Slavin, J. A., Imber, S. M., Gershman, D. J., Raines, J. M., Jackman, C. M., et al. (2015). MESSENGER observations of flux ropes in Mercury's magnetotail. *Planetary and Space Science*, *115*, 77–89. https://doi.org/10.1016/j.pss.2014.12.016

Diego, P., Laurenza, M., Massetti, S., Storini, M., Desorgher, L., & Vainio, R. (2013). Cutoff rigidities calculation for different shapes of the mercury magnetosphere. In *33rd International Cosmic Ray Conference, Rio de Janeiro* (Vol. 5, 1st ed., pp. 3718). Red Hook, NY: Curran Associates, Inc.

Diego, P., Storini, M., Parisi, M., & Cordaro, E. G. (2005). AE-index variability during corotating fast solar wind streams. *Journal of Geophysical Research*, *110*, A06105. https://doi.org/10.1029/2004JA010715

Gosling, J. T., Asbridge, J. R., Bame, S. J., & Feldman, W. C. (1978). Solar wind stream interfaces. *Journal of Geophysical Research*, *83*(A4), 1401–1412. https://doi.org/10.1029/JA083iA04p01401

Gosling, J. T., Hansen, R. T., & Bame, S. J. (1971). Solar wind speed distributions: 1962–1970. *Journal of Geophysical Research*, *76*(7), 1811–1815. https://doi.org/10.1029/JA076i007p01811

Gosling, J. T., Hildner, E., Asbridge, J. R., Bame, S. J., & Feldman, W. C. (1977). Noncompressive density enhancements in the solar wind. *Journal of Geophysical Research*, *82*(32), 5005–5010. https://doi.org/10.1029/JA082i032p05005

Iucci, N., Parisi, M., Storini, M., & Villoresi, G. (1979). High speed solar wind streams and galactic cosmic rays modulation. *Il Nuovo Cimento C*, *2*(4), 421–438. https://doi.org/10.1007/BF02558283

James, M. K., Imber, S. M., Bunce, E. J., Yeoman, T. K., Lockwood, M., Owens, M. J., & Slavin, J. A. (2017). Interplanetary magnetic field properties and variability near Mercury's orbit. *Journal of Geophysical Research: Space Physics*, *122*, 7907–7924. https://doi.org/10.1002/2017JA024435

Johnson, C. L., & Hauck, S. A. (2016). A whole new Mercury: MESSENGER reveals a dynamic planet at the last frontier of the inner solar system. *Journal of Geophysical Research: Planets*, *121*, 2349–2362. https://doi.org/10.1002/2016JE005150

Khabarova, O., & Obridko, V. (2012). Puzzles of the interplanetary magnetic field in the inner heliosphere. *The Astrophysical Journal*, *761*(2), 82. https://doi.org/10.1088/0004-637X/761/2/82

Kivelson, M. G. (2004). Moon-magnetosphere interactions: A tutorial. *Advances in Space Research*, *33*(11), 2061–2077. https://doi.org/10.1016/j.asr.2003.08.042

Klein, L. W., & Burlaga, L. F. (1982). Interplanetary magnetic clouds at 1 AU. *Journal of Geophysical Research*, *87*(A2), 613–624. https://doi.org/10.1029/JA087iA02p00613

Korth, B. J., Thomas, A., Zurbuchen, H., Slavin, J. A., Perri, S., Boardsen, S. A., et al. (2011). The interplanetary magnetic field environment at Mercury's orbit. *Planetary and Space Science*, *59*(15), 2075–2085. https://doi.org/10.1016/j.pss.2010.10.014

Korth, H., Anderson, B. J., Johnson, C. L., Slavin, J. A., Raines, J. M., & Zurbuchen, T. H. (2018). Structure and configuration of Mercury's magnetosphere. In S. Solomon, L. Nittler, & B. Anderson (Eds.), *Mercury: The view after MESSENGER* (Cambridge Planetary Science) (pp. 430–460). Cambridge: Cambridge Univ. Press.

Kumar, A., & Rust, D. M. (1996). Interplanetary magnetic clouds, helicity conservation, and current-core flux-ropes. *Journal of Geophysical Research*, *101*(A7), 15,667–15,684. https://doi.org/10.1029/96JA00544

Leer, E., Holzer, T. E., & Fla, T. (1982). Acceleration of the solar wind. *Space Science Reviews*, *33*(1–2), 161–200. https://doi.org/10.1007/BF00213253

Liu, Y., Richardson, J. D., & Belcher, J. W. (2005). A statistical study of the properties of interplanetary coronal mass ejections from 0.3 to 5.4 AU. *Planetary and Space Science*, *53*(1–3), 3–17. https://doi.org/10.1016/j.pss.2004.09.023

Liu, Y., Richardson, J. D., Belcher, J. W., Kasper, J. C., & Elliott, H. A. (2006). Thermodynamic structure of collisiondominated expanding plasma: Heating of interplanetary coronal mass ejections. *Journal of Geophysical Research*, *111*, A01102. https://doi.org/10.1029/2005JA011329

Lopez, R. E. (1987). Solar cycle invariance in solar wind proton temperature relationships. *Journal of Geophysical Research*, *92*(A10), 11,189–11,194. https://doi.org/10.1029/JA092iA10p11189

Mariani, F., Bavassano, B., & Villante, U. (1983). A statistical study of MHD discontinuities in the inner solar system—HELIOS 1 and 2. *Solar Physics*, *83*(2), 349–365. https://doi.org/10.1007/BF00148285

Mariani, F., Ness, N. F., Burlaga, L. F., Bavassano, B., & Villante, U. (1978). The large-scale structure of the interplanetary magnetic field between 1 and 0.3 AU during the primary mission of Helios 1. *Journal of Geophysical Research*, *83*(A11), 5161–5166. https://doi.org/10.1029/JA083iA11p05161

Mariani, F., Villante, U., Bruno, R., Bavassano, B., & Ness, N. F. (1979). An extended investigation of HELIOS 1 and 2 observations—The interplanetary magnetic field between 0.3 and 1 AU. *Solar Physics*, *63*(2), 411–421. https://doi.org/10.1007/BF00174545

Marsch, E. (1991). Turbulence in the solar wind. In G. Klare (Ed.), *Reviews in modern astronomy* (Vol. 4, pp. 145–156). Berlin: Springer.

Marsch, E., Mühlhäuser, K.-H., Schwenn, R., Rosenbauer, H., Pilipp, W., & Neubauer, F. M. (1982). Solar wind protons: Three-dimensional velocity distributions and derived plasma parameters measured between 0.3 and 1 AU. *Journal of Geophysical Research*, *87*(A1), 52–72. https://doi.org/10.1029/JA087iA01p00052

Martinez, W. L., & Martinez, A. R. (2002). *Computational statistics handbook with MATLAB*. Boca Raton: Chapman & Hall/CRC.

Raines, J. M., DiBraccio, G. A., Cassidy, T. A., Delcourt, D. C., Fujimoto, M., Jia, X., et al. (2015). Plasma sources in planetary magnetospheres: Mercury. *Space Science Reviews*, *192*(1–4), 91–144. https://doi.org/10.1007/s11214-015-0193-4

Richardson, I. G., & Cane, H. V. (2010). Near-Earth interplanetary coronal mass ejections during solar cycle 23 (1996 – 2009): Catalog and summary of properties. *Solar Physics*, *264*(1), 189–237. https://doi.org/10.1007/s11207-010-9568-6

Russell, C. T., Baker, D. N., & Slavin, J. A. (1988). The magnetosphere of mercury. In F. Vilas, C. R. Chapman, & M. S. Matthews (Eds.), *Mercury* (pp. 514–561). Tucson: University of Arizona Press.

Sanchez-Diaz, E., Rouillard, A. P., Lavraud, B., Segura, K., Tao, C., Pinto, R., et al. (2016). The very slow solar wind: Properties, origin and variability. *Journal of Geophysical Research: Space Physics*, *121*, 2830–2841. https://doi.org/10.1002/2016JA022433

Sarantos, M., Reiff, P. H., Hill, T. W., Killen, R. M., & Urquhart, A. L. (2001). A B_x-interconnected magnetosphere model for Mercury. *Planetary and Space Science*, *49*(14–15), 1629–1635. https://doi.org/10.1016/S0032-0633(01)00100-3

Sarantos, M., & Slavin, J. A. (2009). On the possible formation of Alfvén wings at Mercury during encounters with coronal mass ejections. *Geophysical Research Letters*, *36*, L04107. https://doi.org/10.1029/2008GL036747

Schwenn, R. (1990). Large-Scale Structure of the Interplanetary Medium. In R. Schwenn & E. Marsch (Eds.), *Physics of the Inner Heliosphere* (Vol. 1, pp. 99). XI Berlin, Germany: Springer-Verlag.

Scudder, J. D. (2015). Radial variation of the solar wind proton temperature: Heat flow or addition? *The Astrophysical Journal*, *809*(2), 126. https://doi.org/10.1088/0004-637X/809/2/126

Slavin, J. A., Baker, D. N., Gershman, D. J., Ho, G. C., Imber, S. M., Krimigis, S. M., & Sundberg, T. (2018). Mercury's dynamic magnetosphere. In S. Solomon, L. Nittler, & B. Anderson (Eds.), *Mercury: The view after MESSENGER* (Cambridge Planetary Science) (pp. 461–496). Cambridge: Cambridge Univ. Press.

Slavin, J. A., & Holzer, R. E. (1981). Solar wind flow about the terrestrial planets 1. Modeling bow shock position and shape. *Journal of Geophysical Research*, *86*(A13), 11,401–11,418. https://doi.org/10.1029/JA086iA13p11401

Smith, E. J., & Wolfe, J. H. (1979). Fields and plasmas in the outer solar system. *Space Science Reviews*, *23*, 217–252. https://doi.org/10.1007/BF00173811

Villante, U., Bruno, R., Mariani, F., Burlaga, L., & Ness, N. (1979). The shape and location of the sector boundary surface in the inner solar system. *Journal of Geophysical Research*, *84*(A11), 6641–6648. https://doi.org/10.1029/JA084iA11p06641

Villante, U., Mariani, F., Burlaga, L. F., & Ness, N. F. (1978). IMF structures between 0.3 and 1 A.U. A comparison of two-spacecraft observations. *Il Nuovo Cimento C*, *1*(4), 261–274. https://doi.org/10.1007/BF02525040